Chemical Engineering Journal 160 (2010) 239–248

Contents lists available at ScienceDirect

Chemical Engineering Journal

journal homepage: www.elsevier.com/locate/cej

Two-dimensional and three-dimensional computational studies of hydrodynamics in the transition from bubbling to circulating fluidised bed

L.M. Armstrong, K.H. Luo, S. Gu*

Energy Technology Research Group, School of Engineering Sciences, University of Southampton, Southampton, SO17 1BJ, United Kingdom

ARTICLE INFO

Article history:
Received 26 April 2009
Received in revised form 15 February 2010
Accepted 16 February 2010

Keywords:
CFD
Hydrodynamics
Circulating fluidised bed
Eulerian
EMMS

ABSTRACT

This paper applies two-fluid modelling (TFM) to a two-dimensional and three-dimensional circulating fluidised bed (CFB). An energy minimisation multiscale (EMMS) based drag model is compared with a classical drag model, namely the Gidaspow model in the light of experimental data from the CFB. The axial particle velocities and the radial volume fraction at different heights are considered. The specularity coefficient responsible for the tangential solid velocities at the walls is varied to study the effect on the downflow of particles at the wall. The work is further extended to explore the effects of velocity variation on the flow distribution showing the transition from a bubbling to a fast fluidising regime. Furthermore, the diameters of the bubbles observed within the bubbling regime are compared with the Davidson's bubble diameter model for a range of particle diameters. Varying the specularity coefficient showed that a free slip boundary condition underpredicted the downflow of particles at the wall and to add slight roughness to the wall gave a closer representation. The predictions for the 2D and 3D CFB axial velocities were in good agreement with the experimental data but the 2D results slightly overpredicted the core velocity. The transition from a bubbling to a fast fluidising regime as expected occurred once the inlet velocity exceeded the terminal velocity. The equivalent bubble diameter from the simulations agreed well with the calculated bubble diameter from the model.

1. Introduction

The increasing application of circulating fluidised bed (CFB) technology in industry demands optimum reactor designs to improve efficiency and reduce emissions. Examples include cracking, fuel production and power generation [1,2]. Computational fluid dynamic (CFD) modelling has become a viable tool for simulating the dynamic processes that take place in CFBs. Recent increase in computer capabilities allows for non-invasive simulations for complex geometries, and wide parameter ranges to be carried out. Before the accurate simulations of the full reaction processes can be carried out, the basic hydrodynamics of the multiphase flow needs to be thoroughly investigated. The hydrodynamics of fluidised bed reactors has attracted research interest for decades [1–6] although many questions remain especially concerning gas and particle interactions.

Most studies apply the Eulerian–Eulerian two-fluid model (TFM) which assumes the gas–solid phases as continuous and fully interpenetrating within each control volume [1,4,5,7]. It is less computationally exhaustive in comparison to the other models: the discrete Eulerian–Lagrangian method which simulates the individual particle dynamics [8–11], and the complete Lagrangian model which models both particles and fluid with a Lagrangian approach [3,12,13]. However, TFMs have issues with regard to scaling sizes. In order to obtain a sufficient representation of the particle–fluid interactions and structures, small control volumes are required [14]. This method has shown reasonable results for small scale CFBs with a height around 1–2 m as the control volumes are small. However, increasing the dimensions of the reactor would require large cell sizes to reduce computational time and expense resulting in the model's inability to capture the full particle structures [7].

Drag models are important in simulating the interphase momentum transfer between the gas and particle phases. There are a number of average-based drag models available in the literature including the Gidaspow et al. [15], Syamlal and O'Brien [16] and the Wen-Yu [17] drag models. An extensive review of the different averaged-based, non-filtered drag models was carried out previously by Van Wachem et al. [18]. Whilst these models have produced similar results compared to experimental data, they do not take into account the structure of particle clusters at different scales. O'Brien and Syamlal [19] stated that the importance of the clustering of particles needs to be accounted for in current drag correlations. Gunn and Malik [20] determined that for grouped clusters of particles with a given fluid flow rate and voidage, there was a decrease in the measured drag coefficient due to the increase of gas flowing around the clusters and decrease in gas flow penetrating them.

---

* Corresponding author. Tel.: +44 23 8059 4760; fax: +44 23 8059 3058.
E-mail address: s.gu@soton.ac.uk (S. Gu).

1385-8947/$ – see front matter © 2010 Elsevier B.V. All rights reserved.
doi:10.1016/j.cej.2010.02.032

Nomenclature

$\bar{\bar{I}}$	stress tensor
C_D	drag coefficient
d_i	diameter (m)
e	coefficient of restitution
g	acceleration due to gravity ($\mathrm{ms^{-2}}$)
g_0	radial distribution coefficient
h	height (m)
I_{2D}	second invariant of deviatoric stress tensor
k_{Θ_s}	diffusion coefficient (kg/s m)
K_i	momentum interface exchange coefficient
p	gas pressure (Pa)
p_i	phase pressure (Pa)
R, r	radius (m)
Re	Reynolds number
t	time (s)
V_t	terminal velocity ($\mathrm{ms^{-1}}$)

Greek letters

γ_i	collisional dissipation of energy ($\mathrm{kg/s^3\,m}$)
λ_i	bulk viscosity (kg/s m)
μ_i	shear viscosity (kg/s m)
$\bar{\bar{\tau}}_i$	stress tensor (Pa)
ϕ	angle of internal friction (°), Eq. (28)
ϕ	transfer of kinetic energy ($\mathrm{kg/s^3\,m}$)
ρ_i	density ($\mathrm{kg\,m^{-3}}$)
Θ	granular temperature ($\mathrm{m^2\,s^{-2}}$)
υ_i	velocity ($\mathrm{ms^{-1}}$)
ε_i	volume fraction
φ	specularity coefficient

Subscripts

g	gas
i	general index
p	particles
q	phase
s	solids
w	wall

Recently a drag model has been developed using numerical–experimental data from Lattice Boltzmann modelling (LBM). The terminology numerical–experimental is justified by the fact that LBM uses first principle calculations [21]. The Lattice Boltzmann method (LBM) is based on first principles so the derivation of a drag law by Hill et al. [22,23] provided the most extensive numerical–experimental data reported to date [21]. Hill et al. [22,23] developed a number of different formulas for the drag function at varying Reynolds numbers and particle volume fraction. However, the transition of the drag values for the different equations were very sudden and contained gaps between values. Benyahia et al. [21] further extended their models to develop a single composite formula which smoothly covers the varying range of Reynolds numbers and volume fraction without jumps or gaps such that it can be applied to multiphase models which require smooth transitions over ranges.

An alternative approach developed by Zhang and VanderHeyden [24] applied a two-average approach wherein the first-averaged equations obtained from the ensemble phase-average technique [25,26] were averaged a second time repeating this same averaging technique. They found the second average revealed new terms representing the mesoscale effects which would strongly influence the macroscopic behaviour of the flow. The added mass of the mesoscale structures were considered and shown to be important due to local density being proportional to the mixture density instead of the gas density. Furthermore, a significant reduction was observed in the drag coefficient within these mesoscale structures [14,24]. This work has been further extended by De Wilde et al. [27,28] with the reformulation of the added mass closure model. These filtered models are necessary to simulate large-scale reactors due to their effectiveness on course-sized grids [14].

Yang et al. [29] modified a drag model to incorporate the energy minimisation multiscale (EMMS) approach [30]. This approach looks at the phase interactions that take place at three different scales. Micro-scale modelling of the discrete particles in either the dilute phase which is fluid-dominated (FD) and the dense phase which is particle-dominated (PD). Mesoscale modelling of the clusters of particles with the interactions between the dense cluster and the dilute phase, known as particle–fluid compromising (PFC). Macro-scale modelling considers the boundary effects upon the particle–fluid suspensions and interactions. Li et al. [31] found the flow to be heterogeneous in gas–fluid fluidisation and the effects of the boundaries can lead to axial and radial heterogeneity. These heterogeneous structures cause issues when using standard average-based TFM approaches as disparity between the dilute core annulus and dense wall regions is so dramatic. The EMMS drag model has been applied by key researchers within the field of fluidisation hydrodynamics [29,30,32,33,31], calculations were made and compared for the slip velocities and drag coefficients for the different interaction phases of dense clusters, dilute phases and interactions between them both [30]. This was further extended to show the strong dependence of the drag coefficient on simple structural differences [32] and later a decrease in drag coefficient due to local and global structural changes. The standard TFMs only relate the drag coefficients to the local slip velocities and average voidages hence not displaying the overall structural effects.

The Reynolds numbers for the multiphase flows within CFB risers are high so turbulence models have been applied for many years [1,4,5]. The turbulent interaction between the phases and time-averaged turbulent flow behaviour needs to be modelled with the correct closure models and empirical constants in order to accurately simulate more realistic results. Some comparisons between simulations using turbulence models and laminar models suggested that the use of laminar models led to more consistent results over the turbulence models [5]. However, such comparisons were carried out in 2D simulations and since turbulence fluctuations always have three-dimensional spatial character then 3D comparative studies are required to draw a firm conclusion.

The kinetic theory of granular flow is one of the most important tools for modelling the motion of particles. The basic concept of the theory is the granular temperature. During random oscillations of the particles, inelastic collisions occur causing energy to be dissipated. The granular temperature measures these random oscillations of the particles and is defined as the average of the three variances of the particle's velocities. A full mathematical description of the kinetic theory is provided by Gidaspow [34]. Recently, there have been numerous applications of the kinetic theory approach for modelling both BFBs [8,35] and CFBs [1,4–6].

The coefficient of restitution was developed by Jenkins and Savage [36] to account for the loss of energy due to particle collisions. The coefficient quantifies the elasticity of the particle collisions where a value of 0 indicates fully inelastic collisions whilst a coefficient of 1 represents fully elastic collisions. Previous hydrodynamic work has found that decreasing the coefficient of restitution leads to less elastic particle collisions resulting in a higher dissipation of energy as more fluctuating energy is generated [6]. The higher the coefficient of restitution suggests that nearly all the energy is conserved during the collisions of particles which results in an active movement of particles [35]. However, due to the extensive parametric studies available in literature on the restitution coefficient will not be focused on in the present study.

Johnson and Jackson [37] developed a boundary condition that considered the tangential solid velocity and the fluctuating energy at a wall for granular flows. The specularity coefficient, φ, is a parameter used in computational modelling to determine whether the wall is smooth ($\varphi \to 0$) or rough ($\varphi \to 1$) determining the solids tangential velocity imposed at the wall. The parameter will vary depending on a number of factors including the material of the wall, the type of particles used and the sloping/geometry of the walls. However, there are no generic values available in literature which suggest appropriate specularity coefficients depending on such factors, future work on this would be highly advantageous. Fortunately, the specularity coefficient can be altered in for different cases and flow behaviours allowing for good flexibility in results near the boundary. The fluctuation and dissipation of the particle energy due to wall collisions is taken into account by the particle-wall restitution coefficient, e_w.

Three-dimensional modelling has been carried out by several researchers [38–42] with results confirming 3D models to be superior over the 2D models. However, 2D modelling still takes preference over 3D modelling due to the excessive computational time and expense that 3D modelling incurs. With the increase in computational performance and introduction of parallel computing systems, the issues with computational time for 3D modelling are reduced.

The present work compares an isothermal 2D and 3D CFD model using the commercial software FLUENT 6.3.26 with experimental data taken for a CFB [1]. The EMMS-based model developed by Yang et al. [29] is incorporated into the present study as they combined the two-fluid model with the EMMS approach to develop an effective drag coefficient which is applicable to TFM. The effects of the variation of specularity coefficient are considered and the axial particle velocities in the radial direction are compared to experimental results. The volume fraction of particles down a CFB wall is computed. The regimes of fluidisation are explored for a range of inlet velocities with the size of air bubbles within the bubbling regime compared with Davidson's model [43].

2. Experimental setup

The laboratory reactor used for the experiment is provided in more detail by Samuelsberg and Hjertager [1]. Fig. 1 shows a sketch of the experimental setup. The root mean square velocities of the particles were taken at three heights, 0.16 m, 0.32 m and 0.48 m in the reactor using LDA technology. Once fluidised, the particles would travel up the reactor and into the cyclone. Gas would exit from the top of the cyclone whilst particles descend down the downcomer to be re-introduced into the reactor. An initial static bed height for the catalyst particles was 0.05 m with a secondary air inlet position at the same height. The secondary inlet forced circulating particles back into the reactor.

FCC particles were used with a density of 1600 kg/m^3 and a diameter range 20–150 μm. The mean diameter was taken to be 60 μm. Two superficial gas velocities were introduced through the primary inlet, 0.71 ms^{-1} and 1.42 ms^{-1} at an ambient temperature. The secondary inlet introduced air at a constant rate of 0.05 ms^{-1}.

3. CFD modelling

3.1. Mesh production

The complete two-dimensional CFB mesh consisted of 57,680 quadrilateral cells. The cells in the vertical direction were uniformly distributed with a cell size of 0.001 m. To capture the complex flow behaviours at the walls, the nodes in the radial direction were non-uniformly distributed with a more refined grid near the walls. The cell sizes in the horizontal direction range from a minimum of 0.0005 m up to a maximum of 0.001 m. The 3D mesh contained 1,620,798 cells with the horizontal cell sizes ranging from a minimum of 0.00075 m to a maximum of 0.002 m. To reduce the computational cost, the 3D grid is coarser than the 2D grid. A study of the grid size dependence is described in Appendix A.

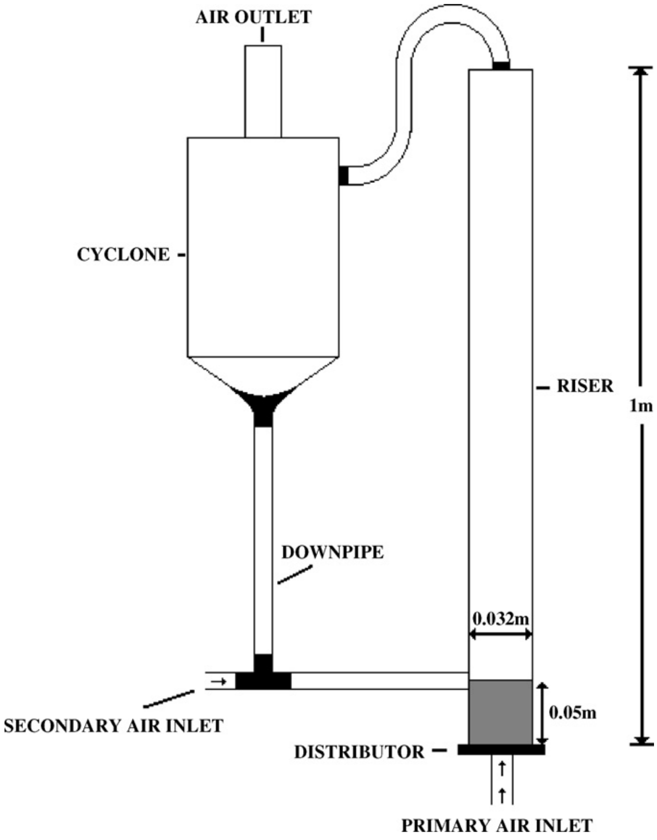

Fig. 1. Sketch of the laboratory scale circulating fluidised bed used in literature [1].

Two fluidising regimes are considered, fast fluidising and bubbling. The bubbling bed uses the same diameter as the CFB riser taken from the literature [1] however to reduce the computational time and expense the simulations are carried out with only halve the height, 0.5 m. The secondary inlet is not present in the bubbling bed therefore the mesh contains the primary inlet, riser and a pressure outlet set 0.5 m above the inlet. The 2D and 3D meshes contained 18,732 cells and 733,821 cells, respectively, with the cell sizes taken from the CFB measurements above.

3.2. Governing equations

The Eulerian-granular model in FLUENT 6.3.26 is used to model the interactions between gas and granular particles within this fluidised bed. This model allows for the presence of two different phases in one control volume of the grid by introducing the volume fraction variable. The solid phase contains spherical granular particles of the same diameter. These two phases are solved individually using the mass and momentum equations. Table 1 gives details of the full equations. The energy equation is ignored in this case as the flow is isothermal as are the virtual mass and lift effects. This is because lift only affects particles of large diameters and this is not the present case. For larger Reynolds numbers, the κ–ε turbulence model is used to model the gaseous phase. The transport equations for κ and ε are given in Table 1. The model constants are

Table 1
Governing equations.

Conservation of mass	Equation
Gas	
$\frac{\partial(\varepsilon_g \rho_g)}{\partial t} + \nabla \cdot (\varepsilon_g \rho_g \vec{\upsilon}_g) = 0$	(1)
Particle	
$\frac{\partial(\varepsilon_s \rho_s)}{\partial t} + \nabla \cdot (\varepsilon_s \rho_s \vec{\upsilon}_s) = 0$	(2)
Conservation of momentum	
Gas	
$\frac{\partial\left(\varepsilon_g \rho_g \vec{\upsilon}_g\right)}{\partial t} + \nabla \cdot (\varepsilon_g \rho_g (\vec{\upsilon}_g \otimes \vec{\upsilon}_g)) =$ $-\varepsilon_g \nabla p + \nabla \cdot \bar{\bar{\tau}}_g + \varepsilon_g \rho_g \vec{g} + K_{gs} (\vec{\upsilon}_g - \vec{\upsilon}_s)$	(3)
Particle	
$\frac{\partial(\varepsilon_s \rho_s \vec{\upsilon}_s)}{\partial t} + \nabla \cdot (\varepsilon_s \rho_s (\vec{\upsilon}_s \otimes \vec{\upsilon}_s)) =$ $-\varepsilon_s \nabla p - \nabla p_s + \nabla \cdot \bar{\bar{\tau}}_s + \varepsilon_s \rho_g \vec{g} + K_{gs} (\vec{\upsilon}_g - \vec{\upsilon}_s)$	(4)
Phase stress–strain tensor	
$\bar{\bar{\tau}}_q = \varepsilon_q \mu_q \left(\nabla \vec{\upsilon}_q + \nabla \vec{\upsilon}_q^T\right) + \varepsilon_q \left(\lambda_q - \frac{2}{3}\mu_q\right) \nabla \cdot \vec{\upsilon}_q \bar{\bar{I}}_q$	(5)
Gas turbulent modelling	
$\frac{\partial\left(\alpha_g \rho_g \kappa\right)}{\partial t} + \nabla \cdot (\alpha_g \rho_g \vec{\upsilon}_g \kappa) = \nabla \cdot \alpha_g \left(\mu_{gl} + \frac{\mu_{g_t}}{\sigma_\kappa} \nabla \cdot \kappa\right) + \alpha_g G_\kappa - \alpha_g \rho_g \varepsilon$ $\frac{\partial\left(\alpha_g \rho_g \epsilon\right)}{\partial t} + \nabla \cdot (\alpha_g \rho_g \vec{\upsilon}_g \varepsilon) =$ $\nabla \cdot \alpha_g \left(\mu_{g_l} + \frac{\mu_{g_t}}{\sigma_\varepsilon} \nabla \cdot \varepsilon\right) + \frac{\alpha_g \varepsilon}{\kappa} \left(C_{\varepsilon_1} G_\kappa - C_{\varepsilon_2} \rho_g \varepsilon\right)$ $\mu_g = \mu_{g_l} + \mu_{g_t}$ $\mu_{g_t} = \rho_g C_\mu \frac{\kappa^2}{\varepsilon}$ $G_\kappa = \mu_{g_t} \nabla \vec{\upsilon}_g \cdot \left[\nabla \vec{\upsilon}_g + (\nabla \vec{\upsilon}_g)^T\right] - \frac{2}{3} \nabla \vec{\upsilon}_g \left(\mu_{g_t} \nabla \vec{\upsilon}_g + \rho_g \kappa\right)$	
Kinetic fluctuation energy	
$\frac{3}{2}\left[\frac{\partial}{\partial t}\left(\varepsilon_s \rho_s \Theta_s\right) + \nabla \cdot \left(\varepsilon_s \rho_s \vec{\upsilon}_s \Theta_s\right)\right] = \left(-p_s \cdot \bar{\bar{I}} + \bar{\bar{\tau}}_s\right) :$ $\nabla \vec{\upsilon}_s + \nabla \cdot \left(k_{\Theta_s} \cdot \nabla \Theta_s\right) - \gamma_{\Theta_s} + \phi_{gs}$	(6)
$k_{\Theta_s} = \frac{150 \rho_s d_s \sqrt{\Theta_s \pi}}{384(1+e) g_0} \left[1 + \frac{6}{5} \varepsilon_s g_0 (1+e)\right]^2 + 2\varepsilon_s^2 \rho_s d_s (1+e) g_0 \sqrt{\frac{\Theta_s}{\pi}}$	(7)
$\gamma_{\Theta_s} = \frac{12(1-e)^2 g_0}{d_s \sqrt{\pi}} \varepsilon_s^2 \rho_s \Theta_s^{3/2}$	(8)
$\phi_{gs} = -3 K_{gs} \Theta_s$	(9)
Definitions	
$\varepsilon_g + \varepsilon_s = 1$	(10)

$C_{\varepsilon_1} = 1.44$, $C_{\varepsilon_2} = 1.92$ and $C_\mu = 0.09$. The turbulent Prandtl numbers for κ and ε are $\sigma_\kappa = 1.0$ and $\sigma_\varepsilon = 1.3$ respectively. μ_{g_t} defines the turbulence viscosity and G_κ represents the generation of turbulent kinetic energy due to the mean velocity gradients.

The kinetic fluctuations between particles are considered using the kinetic theory of granular flow given in Table 1. The solid shear viscosity is composed of collisional, kinetic and frictional effects. For very dense flows, frictional viscosity is applied due to the volume fraction for the particles approaching the packing limit. Schaeffer's expression [44] is used to model the frictional viscosity in dense cases. The bulk viscosity accounts for the resistance of particle to expansion and depression and is calculated using an expression from Lun et al. [45]. The solids pressure is composed of two terms, where the first term represents the kinetic term and the second term is due to particle collisions. It was determined from an equation of state which was similar to the van der Waals equation of state for gases [46]. The radial distribution function modifies the probability of particle collisions as the phase becomes dense. Table 3 contains the equations for these constitutive equations.

Table 2
Momentum interphase exchange coefficient.

Momentum interphase exchange coefficient	Equation
Gidaspow drag model	
$K_{gs} = 150 \frac{\varepsilon_s^2 \mu_g}{\varepsilon_g d_s^2} + 1.75 \frac{\varepsilon_s \rho_g \lvert\vec{\upsilon}_s - \vec{\upsilon}_g\rvert}{d_s}$	(11)
for $\varepsilon_g \le 0.8$	
$K_{gs} = \frac{3}{4} C_D \frac{\varepsilon_s \varepsilon_g \rho_g \lvert\vec{\upsilon}_s - \vec{\upsilon}_g\rvert}{d_s} \varepsilon_g^{-2.65}$ for $\varepsilon_g > 0.8$	(12)
$C_D = \frac{24}{\varepsilon_g Re_s}\left[1 + 0.15(\varepsilon_g Re_s)^{0.687}\right]$	(13)
EMMS-based drag model	
$K_{gs} = 150 \frac{\varepsilon_s^2 \mu_g}{\varepsilon_g^2 d_s^2} + 1.75 \frac{\varepsilon_s \rho_g \lvert\vec{\upsilon}_s - \vec{\upsilon}_g\rvert}{\varepsilon_g d_s}$	(14)
for $\varepsilon_g \le 0.8$	
$K_{gs} = \frac{3}{4} C_D \frac{\varepsilon_s \rho_g \lvert\vec{\upsilon}_s - \vec{\upsilon}_g\rvert}{d_s} \omega(\varepsilon)$ for $\varepsilon_g > 0.8$	(15)
$\omega(\varepsilon) =$ $\begin{cases} -0.5760 + \dfrac{0.0214}{4(\varepsilon_g - 0.7463)^2 + 0.0044} & (0.74 < \varepsilon_g \le 0.82) \\ -0.0101 + \dfrac{0.0038}{4(\varepsilon_g - 0.7789)^2 + 0.0040} & (0.82 < \varepsilon_g \le 0.97) \\ -31.8295 + 32.8295\varepsilon_g & (\varepsilon_g > 0.97) \end{cases}$	(16)
$C_D = \frac{24}{Re_s}\left[1 + 0.15(Re_s)^{0.687}\right]$ for $Re_s \le 1000$	(17)
$C_D = 0.44$ for $Re_s > 1000$	(18)
$Re_s = \frac{\rho_g d_s \lvert\vec{\upsilon}_s - \vec{\upsilon}_g\rvert}{\mu_g}$	(19)

Table 3
Constitutive equations.

Constitutive equations	Equation
Solids shear viscosity: $\mu_s = \mu_{s,\mathrm{col}} + \mu_{s,\mathrm{kin}} + \mu_{s,\mathrm{fr}}$	(20)
Collisional viscosity: $\mu_{s,\mathrm{col}} = \frac{4}{5} \varepsilon_s d_s \rho_s g_0 (1+e) \left(\frac{\Theta_s}{\pi}\right)^{1/2}$	(21)
Kinetic viscosity: $\mu_{s,\mathrm{kin}} = \frac{10 d_s \rho_s \sqrt{\Theta_s \pi}}{96 \varepsilon_s g_0 (1+e)} \left[1 + \frac{4}{5} \varepsilon_s g_0 (1+e)\right]^2$	(22)
Frictional viscosity: $\mu_{s,\mathrm{fr}} = \frac{p_s \sin\phi}{2\sqrt{I_{2D}}}$	(23)
Solid bulk viscosity: $\lambda_s = \frac{4}{3} \varepsilon_s d_s \rho_s g_0 (1+e) \left(\frac{\Theta_s}{\pi}\right)^{1/2}$	(24)
Particle pressure: $p_s = \varepsilon_s \rho_s \Theta_s + 2\rho_s (1+e) \varepsilon_s^2 g_0 \Theta_s$	(25)
Radial distribution function: $g_0 = \left[1 - \left(\frac{\varepsilon_s}{\varepsilon_{s,\mathrm{max}}}\right)^{1/3}\right]^{-1}$	(26)

The gas–solid momentum exchange coefficient within the CFB is modelled initially using the Gidaspow drag function as in Table 2. This drag function is applicable to both dense and dilute systems. The CFB is modelled further to account for particle clustering at multiscales by implementing the simplified EMMS-based model (in Table 2) developed by Yang et al. [29] into Fluent with User-Defined Functions (UDF). The gas–solid momentum interphase exchange coefficient, K_{gs}, was modelled for the BFB using the Gidaspow drag model.

The finite volume method was used to solve the governing equations. The coupling and correction of the velocity and pressure is carried out for multiphase flows with the Phase Coupled SIMPLE (PCSIMPLE) algorithm [47]. The discretisation of the convective terms was carried out with the second-order upwind scheme. A time step of 1×10^{-4} was used to ensure quick convergence with 30 iterations per time step. The convergence criterion between two iterations was set to 1×10^{-3}.

3.3. *Boundary and initial conditions*

The particle bed is initially set to a height of 0.05 m above the main inlet with particles set to a diameter of 60 μm and density of 1600 kg/m^3. There are two gas inlets, the main inlet providing constant gas supply with velocities between 0.06 ms^{-1} and 1.42 ms^{-1}, and a secondary inlet during the CFB simulation set to 0.05 ms^{-1} to prevent backflow of particles within the re-entry tube. A pressure outlet was used with no solid particles allowed to leave the

Table 4
Boundary conditions.

Particle Phase Boundary Conditions	
Velocity	
$\vec{u}_{s,w} = -\frac{6\mu_s \varepsilon_{s,\mathrm{max}}}{\sqrt{3}\sqrt{\theta}\pi\varphi\rho_s\varepsilon_s g_0} \frac{\partial \vec{\upsilon}_{s,w}}{\partial n}$	(27)
Granular temperature	
$\theta_w = -\frac{\kappa\theta}{\gamma_w} \frac{\partial\theta}{\partial n} + \frac{\sqrt{3}\pi\varphi\rho_s\varepsilon_s g_0 \vec{\upsilon}_{s,slip}^2 \theta^{\frac{3}{2}}}{6\gamma_w \varepsilon_{s,max}}$	(28)
$\gamma_w = \frac{\sqrt{3}\pi\left(1 - e_w^2\right)\varepsilon_s \rho_s g_0 \theta^{\frac{3}{2}}}{4\varepsilon_{s,\mathrm{max}}}$	(29)

Table 5
Table of parameters.

Gas		
υ_g	Velocity	(0.06–1.42)ms^{-1}
ρ_g	Density	1.225 kgm^{-3}
μ_g	Shear viscosity	1.79×10^{-5} kg/m s
Particles		
d_p	Particle diameter	40, 60, 80 μm
ρ_p	Particle density	1600 kgm^{-3}
e	Particle coefficient of restitution	0.995
e_w	Wall coefficient of restitution	0.95
φ	Specularity coefficient	0, 0.25, 0.5, 0.75, 1.0

reactor. In the case of BFB, the secondary inlet is replaced with wall.

Table 3.

The effects of particle-wall collisions within CFB risers play a significant part on the shear stress at the walls. The boundary conditions at the walls for the gas phase have tangential and normal velocities of zero, namely no-slip boundary conditions. For the par-

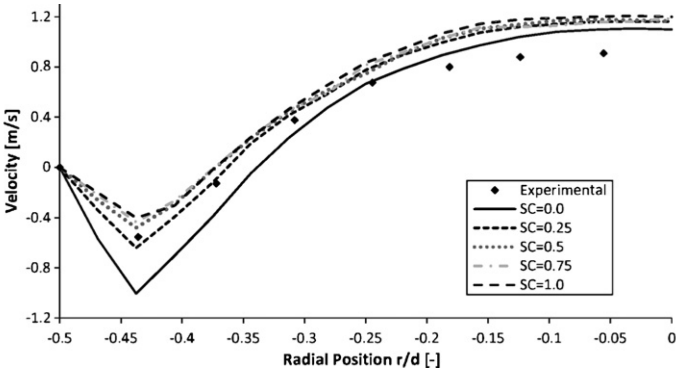

Fig. 2. Specularity coefficient effects on axial velocity predictions across the height 0.16 m for d_p =60 μm and V = 0.71 ms^{-1}.

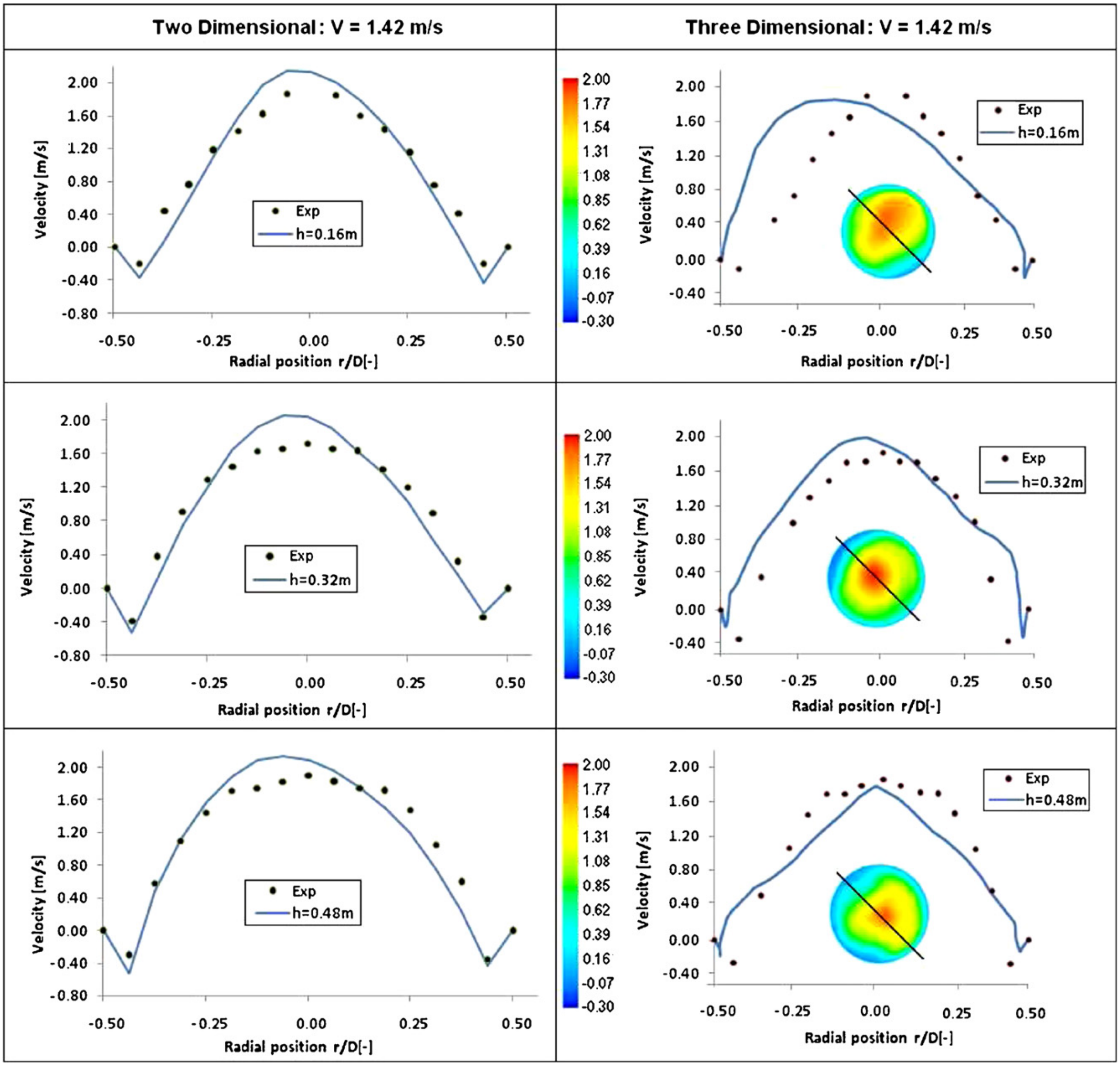

Fig. 3. 2D and 3D axial velocities particles at different radial positions for the EMMS-based model with inlet velocity, V = 1.42 ms^{-1}, across different heights.

ticulate phase, a tangential slip condition is imposed which was developed by Johnson and Jackson [37]. The granular temperature is found by equating the granular temperature flux to the wall and the generation of granular temperature at the wall to the energy dissipation due to particle-wall collisions. Table 4 shows the equations used to model the slip of particles and granular temperature against the wall. The parameters used within the simulations are provided in Table 5.

4. Results and discussion

4.1. Specularity coefficient

A preliminary 2D model was carried out to determine a value for the specularity coefficient which agrees well with the experimental results. The previous model carried out in the literature assumed to allow free slip at the walls and they found that the downflow of particles at the wall was underpredicted. Time-averaged measurements of the local axial velocities were taken at 32 points across the riser at intervals of 0.001 m over a period of 3.0 s once complete circulation had begun. Five specularity coefficients, 0, 0.25, 0.5, 0.75 and 1.0 were set to account for different slip boundary conditions for the solids tangential velocity against the wall. The time-averaged results for an inlet velocity, $V = 0.71\,\mathrm{ms}^{-1}$ and particle diameter, $d_p = 60\,\mu\mathrm{m}$ across the height 0.16 m are shown in Fig. 2. A specularity coefficient of 0 representing free slip at the wall shows an underprediction of the downflow of particles at the wall which concurred with the results given in the literature [1]. Increasing the specularity coefficient reduced the slip at the wall reducing the downflow of particles. In all cases, the velocity within the core of the riser was overpredicted as was also observed in the literature [1]. The specularity coefficient around 0.25 showed a reasonable reproduction of the experimental data for all models carried out and hence chosen to be the specularity coefficient for subsequent simulations.

4.2. Two-dimensional vs three-dimensional simulations

Two-dimensional and three-dimensional simulations of the axial velocities for the fast EMMS-based model are shown in Fig. 3. For both models the results are extracted from 18 points across the heights 0.16 m, 0.32 m and 0.48 m and compared with experimental data from the literature [1]. The experimental data appeared to be taken from half the diameter and replicated symmetrically. The 2D results were time-averaged over a period of 3.0 s once complete circulation had begun. The time-averaged 2D results shows a good comparison of the axial velocity of the particles near the wall which is an improvement on the results seen in the literature [1]. The velocity magnitude however is slightly overpredicted in the core of the riser which was also observed in the literature [1].

For the 3D model, instantaneous results were taken due to the very high computational cost of extracting data at specific points at each time step. The results were taken from a 45–225° line through the riser. The 3D models show that the EMMS-based model has slight asymmetry due to the transient flow structure and the results being taken instantaneously. If the results were time-averaged over a longer period as the 2D results were, then asymmetry would be reduced. Although the results are taken instantaneously there is a clear indication once averaged the velocity magnitude agrees reasonably well with the experimental results. The downflow at the wall is slightly underpredicted which could be due to a number of factors including the results not being time-averaged or a slightly coarser mesh at the walls for the 3D model compared to the 2D model. Variation of the specularity coefficient could improve the downflow particle velocity so a specularity coefficient study for a 3D model is required to determine which value of specularity coefficient works well for a coarser 3D model since the value $\varphi = 0.25$ was determined for the 2D model.

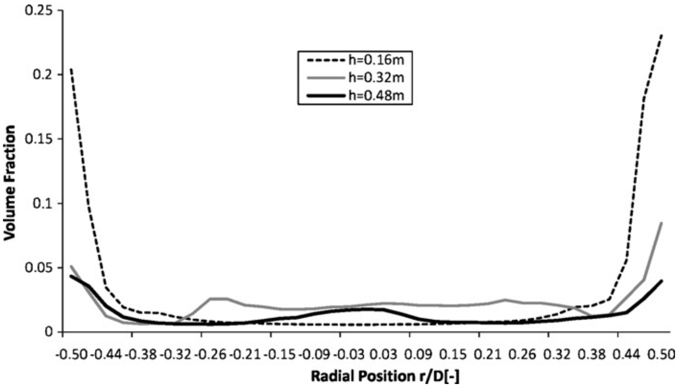

Fig. 4. Radial profiles of particle volume fraction at heights of 0.16 m, 0.32 m and 0.48 m for $d_p = 60\,\mu\mathrm{m}$ and $V = 1.42\,\mathrm{ms}^{-1}$.

Fig. 4 displays the instantaneous volume fraction of particles at the walls across the three heights at time $t = 14.0$ s for the EMMS-based model. The volume fraction at the walls is higher at the lower height as particles continually descend down the walls whilst accumulating more particles from the core. Within the centre of the riser the volume fraction is very dilute with the volume fraction $\varepsilon_s < 0.05$. There is a slight increase in volume fraction within the core at the higher heights as the dispersed particles are carried with the flow however the volume fraction at the higher height, 0.48 m is lower than at 0.32 m probably due to particle segregation towards to wall before it reaches the height 0.48 m. The values are however significantly lower than the regions against the wall. The volume fraction of particles at the wall decreases with height as the particles segregate, descend and collect at the lower heights. Time-averaged results would display a more uniform distribution as any transient flow behaviour would be averaged out.

4.3. Transitional flow results

The 3D simulations were run for over 10.0 s to allow for complete circulation. Fig. 5 shows contour plots of the axial particle velocities and the volume fraction for the two drag models across the reactor at three heights 0.16 m, 0.32 m and 0.48 m for the inlet velocities $0.71\,\mathrm{ms}^{-1}$ and $1.42\,\mathrm{ms}^{-1}$. The results show the presence of asymmetry with faster peak velocities particularly for the Gidaspow drag model. This confirms that transitional effects would influence the flow structure and particle distribution as an inlet velocity of $1.42\,\mathrm{ms}^{-1}$ enters the transitional state. The asymmetric velocities for the Gidaspow drag model are more apparent in the 3D results compared to the 2D results in the literature [1]. The position of the secondary air inlet shows a slight influence on the flow for inlet velocity $0.71\,\mathrm{ms}^{-1}$ at 0.16 m for the Gidaspow and inlet velocities of $0.71\,\mathrm{ms}^{-1}$ and $1.42\,\mathrm{ms}^{-1}$ for the EMMS-based model. The flow starts to centralise with height, as expected. An overprediction of the axial particle velocities for the Gidaspow model would confirm that a collection of particles at the walls reduces the core diameter for the flow to pass which would increase flow velocity. The downflow velocity of particles against the wall shows the majority of particles are falling at the wall down to $-0.532\,\mathrm{ms}^{-1}$; whilst the downflow velocity of particles for the EMMS model shows a lower value of around $-0.32\,\mathrm{ms}^{-1}$ which agrees with the experimental results. The author would like to remind the reader that the 3D models were coarser than the 2D models so the accuracy of the Gidaspow model would be reduced significantly which could also explain the models inaccurate flow velocities compared

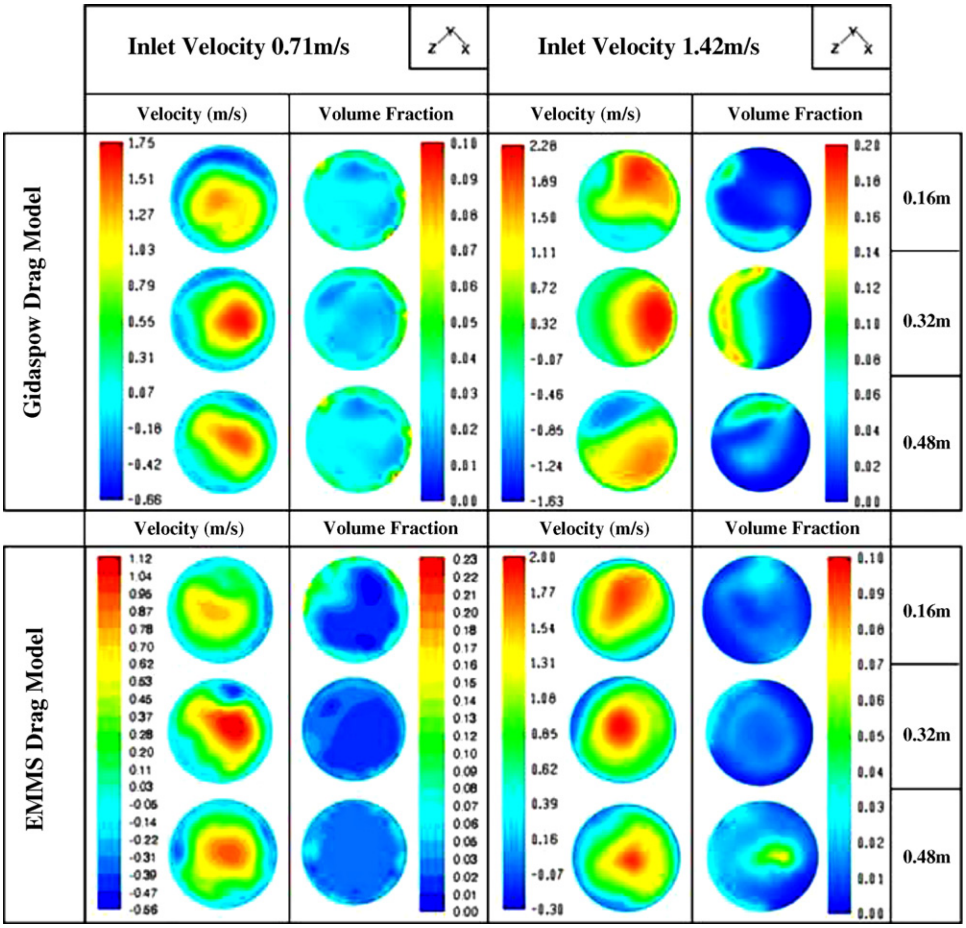

Fig. 5. Comparison of the 3D axial velocities and volume fraction of particles across the heights 0.16 m, 0.32 m and 0.48 m for d_p =60 μm and velocities $V = 0.71\,\text{ms}^{-1}$ and $V = 1.42\,\text{ms}^{-1}$.

to the EMMS-based model which can be applied on coarser grids.

The volume fraction distributions in Fig. 5 for all cases show the accumulation of particles towards the walls. The lower inlet velocities led to a more concentrated and even distribution of particles around the walls of the riser and a lower concentration within the central region where the velocities are high. At lower heights the volume fraction of particles against the walls is larger due to the continual collection of descending particles. At higher inlet velocities, high particle concentration is not always seen at the lower heights or near the walls. The Gidaspow drag model at the $1.42\,\text{ms}^{-1}$ inlet velocity shows a large collection of particles in certain regions, which are not always against the walls. The EMMS-based predicts more uniform particle distribution over the cross-sections of the riser. Interestingly, the highest concentration of particles occurs at a height of 0.48 m. These results confirm that higher inlet velocities reduce the wall effects on particle concentration and can carry particle clusters to higher heights.

4.4. Effects of inlet velocities

The volume fraction distribution for the particles using the Gidaspow drag model with four inlet velocities are shown in Fig. 6(a–d). For particles with a diameter 60 μm, the terminal velocity, V_t, is $0.175\,\text{ms}^{-1}$ so inlet velocities were chosen to capture the behaviour of the particles below and above V_t. Although the terminal velocity applies to single particles in suspension, the bursting-bubbles at the top of the particle bed release a small number of particles above the bed where they are effectively suspended. If the gas velocity does not exceed V_t the particles fall back down to the particle bed. This is referred to as a bubbling bed and is displayed in Fig. 6(a and b). Exceeding V_t means the suspended particles can be carried with the gas phase and continue up the riser. This fast fluidisation state can be seen in Fig. 6(c and d).

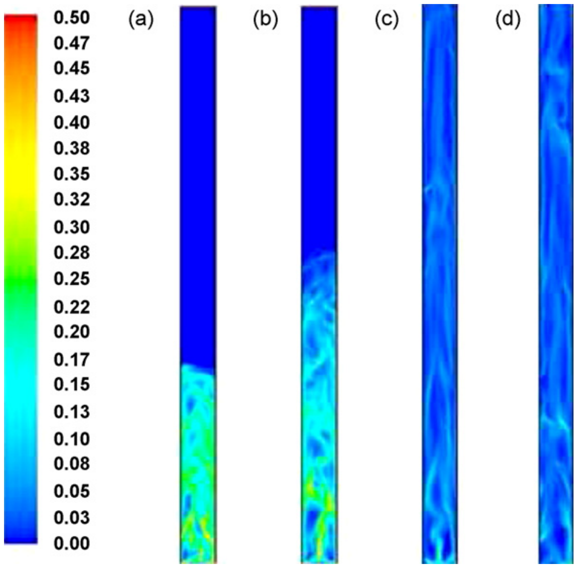

Fig. 6. Volume fraction of particles at 9.0 s for a range of velocities above and below the terminal velocity. For $d_p = 60$ μm: (a) $V = 0.1\,\text{ms}^{-1}$, (b) $V = 0.16\,\text{ms}^{-1}$, (c) $V = 0.18\,\text{ms}^{-1}$ and (d) $V = 0.36\,\text{ms}^{-1}$.

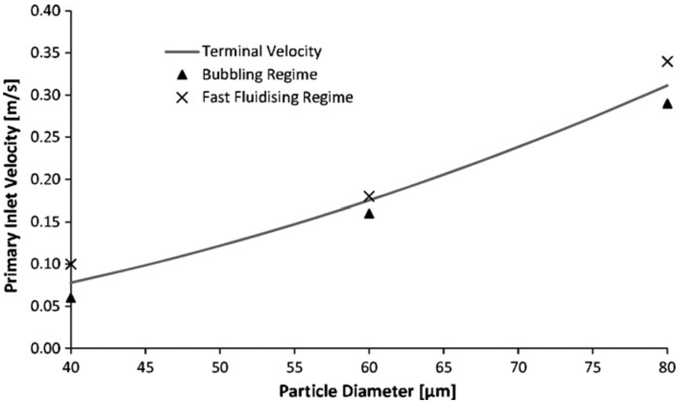

Fig. 7. Fast fluidising regimes observed above the terminal velocity, V_t, and bubbling fluidised regimes below the V_t.

The bed height expansions for the bubbling fluidised states are approximately 0.16 m and 0.3 m for 0.1 ms^{-1} and 0.16 ms^{-1}, respectively. Their contour plots show bubbles appear smaller and more regular shaped near the entrance of the riser, increasing in size and distorting with increasing height. This is due to the coalescence of the bubbles with smaller bubbles rising from the base of the reactor. As the velocity increases, the bubble size increases and the solid–gas mixture appears more dilute particularly towards the top of the bed. The solids descend to the base of the reactor as the solids and gas reach a dynamic equilibrium.

The fast fluidising states in Fig. 6(c and d) shows a dilute regime in comparison to the bubbling regimes. In fast fluidising cases using the standard Gidaspow model, the effects of clustering can not be modelled as accurately as the EMMS model as it does not compensate for the effect of particle clustering at multiscales [19]. The lower velocity 0.18 ms^{-1} shows a higher accumulation of particles nearer the inlet as the inlet velocity is only slightly higher than the terminal velocity.

The simulation was also carried out for different particle diameters of 40 μm and 80 μm. The inlet velocities for the three different diameters are plotted in Fig. 7 and coloured to show the fast fluidising regimes occurring above V_t and bubbling regimes lying below V_t.

4.4.1. Three-dimensional bubbling fluidised beds

Three-dimensional BFB models were performed on three cases; case 1: $d_p = 40\,\mu\text{m}$ with $V = 0.06\,\text{ms}^{-1}$, case 2: $d_p = 60\,\mu\text{m}$ with $V = 0.16\,\text{ms}^{-1}$ and case 3: $d_p = 80\,\mu\text{m}$ with $V = 0.29\,\text{ms}^{-1}$. Fig. 8 shows a slice taken in the *XY* plane (Z=0) for all three cases up to the height 0.3 m above the distributor. Five slices were also taken in the *XZ* plane at different heights depending on the height of the bed in the specific case.

Table 6
Comparison of the equivalent bubble diameter for different particle diameters with the Davidson's model [43].

Diameter (μm)	Equivalent bubble diameter (m)	Davidson's model bubble diameter (m)
40	0.013±0.007	0.01463
60	0.019±0.006	0.02168
80	0.025±0.006	0.02751

The results for case 1 are shown in Fig. 8(a). The *XY* slice through the centre of the bed shows the bed height is approximately 0.12 m. The horizontal slices were taken at heights 0.025 m, 0.05 m, 0.075 m, 0.1 m and 0.12 m. Fig. 8(b) presents the results for case 2 where the *XY* slice through the centre of the bed shows the bed height is approximately 0.17 m. The horizontal slices were taken at heights 0.04 m, 0.08 m, 0.12 m, 0.16 m and 0.18 m. The results for case 3 are shown in Fig. 8(c) with the bed height at approximately 0.26 m. The horizontal slices were taken at heights 0.06 m, 0.12 m, 0.18 m, 0.24 m and 0.28 m.

The model with particle diameter 40 μm shows a high volume fraction of particles overall compared to the other two cases. In all three of the 3D cases the bubble sizes are seen to be larger and more regular in shape at higher heights compared to near the inlet where there is an irregular distribution of solid and voidages. This agrees with the 2D results as the solids and gas compromise for space before coalescence and segregation of particles occurs with increasing height.

The equivalent bubble diameter was calculated for each case using the Davidson's model [43]. The equivalent bubble diameters were taken from the simulations after fluidisation was complete at different heights to account for the smaller bubbles at the base and larger bubbles increasing with height. The results are shown in Table 6. Although Davidson's model assumes the bubbles to be of uniform size distribution, which is not the case here as the velocities are close to the terminal velocity, the results agree well with the average equivalent bubble diameters.

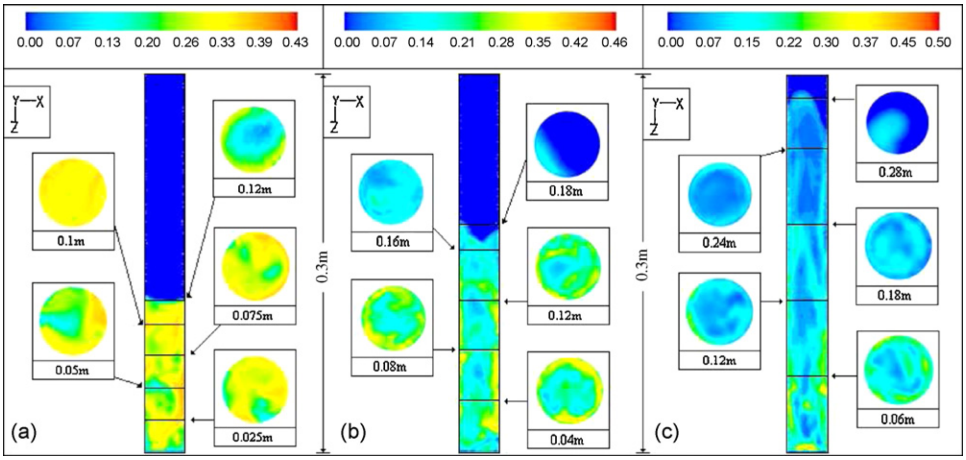

Fig. 8. Contour plots of volume fraction taken through the centre of the reactor and horizontal slices across the reactor at different heights for three cases. (a) $d_p = 40\,\mu\text{m}$ with $V = 0.06\,\text{ms}^{-1}$, (b) $d_p = 60\,\mu\text{m}$ with $V = 0.16\,\text{ms}^{-1}$ and (c) $d_p = 80\,\mu\text{m}$ with $V = 0.29\,\text{ms}^{-1}$.

Table A.1
Table displaying the different grid size cases.

	$\Delta x_{\min}$	$\Delta x_{\max}$	Δy
Case 1	0.001	0.0034	0.01
Case 2	0.00075	0.002	0.005
Case 3	0.0005	0.001	0.001
Case 4	0.00025	0.0005	0.0005

5. Conclusion

Two-dimensional and three-dimensional simulations were carried out on a circulating fluidised bed. Wall effects were considered by adjusting the specularity coefficient. The results showed that a free slip value $\varphi = 0$ underpredicted the axial velocity of the particles at the wall which was also seen in the literature [1]. Increasing this value to 0.25 or 0.5 produced more reliable results. The complete CFB geometry was simulated for a fast fluidising regime using two drag models, the Gidaspow and the energy minimisation multiscale model. The EMMS-based model displays reasonable 3D results with regards to the segregation of particles at the wall and axial velocity distribution this may be due to the 3D models being carried out on coarser meshes which the sub-grid scale model can be applied. The results for the Gidaspow model were not as accurate as a result of the coarseness of the mesh. An instantaneous 2D line taken across the 3D EMMS-based models showed the magnitude of the results agreed fairly well with the 2D experimental results taken from the literature [1] and the time-averaged results from 2D simulation. The volume fraction distribution of particles at three heights within the riser shows an increased collection of particles against the walls at lower heights as the particles descend. The 3D results agreed that higher volume fractions of particles are found at the walls, as seen experimentally and in the 2D models. Increasing the airflow to a transitional state along with the presence of the secondary inlet affects the flow of particles within the bed to produce an irregular flow lower down the riser becoming more regular with height. The transition from a bubbling bed regime to a fast fluidising regime was also considered for a variety of inlet velocities using the riser of the CFB. The results were as expected with the transition from bubbling to fast fluidising regimes occurring after the inlet velocity exceeded the terminal velocity. Within the bubbling regime, bubble size increased with height and with inlet velocity and particle diameter. This was confirmed by comparing the average bubble diameter with Davidson's model [43].

Appendix A. Grid dependency

A 2D grid dependency test was carried using four different grid sizes for the Gidaspow model since it requires finer cells to capture the important flow dynamics. The EMMS model, however, is a sub-grid scale model which can be applied to larger cells in order to capture some of the mesoscale structures. This is a good advantage for larger scaled reactors where smaller grid sizes are far too computationally exhaustive. Table A.1 shows the different grid sizes that were considered. Case 1 replicates the mesh used by Samuelsberg and Hjertager [1] and the meshes in the other cases are refined further until the results show independency. These tests were carried out using the same setup as that seen in the literature [1] with free slip along the walls, $\varphi = 0$. Time-averaged measurements of the local axial velocities were taken at different points across the riser over a period of 3.0 s once complete circulation had begun. The time step remained at 1×10^{-4} for the grid checks since the simulations showed convergence in all grid cases. Although reducing the time step could further improve convergence and could result in slight alteration in the flow dynamics the increase of time for the simulation to reach circulation for the complete bed including cyclone etc. would not be feasible. Fig. A.1 shows the axial particle velocities across the 0.16 m height for the 4 grid sized simulations using an inlet velocity of $V = 0.36\,\mathrm{m\,s^{-1}}$. Although the four cases display similar reasonable results the more refined the mesh the more the results converge as expected. All subsequent 2D models were carried out using the case 3 mesh and the case 2 mesh was used for the 3D mesh. Although it is computationally exhaustive to repeat 3D models for the benefit of determining grid independency it would be highly beneficial to carry out on 3D test instead of relying on the grid independency results of 2D modelling. Furthermore, a full grid dependency for the EMMS-based model on coarser grids would also be beneficial to capture the mesoscale structures, namely clusters and streamers of particles, since these mesoscale structures can be found up to 100 particle diameters—much larger than the cell sizes used for standard drag models [48,34,14].

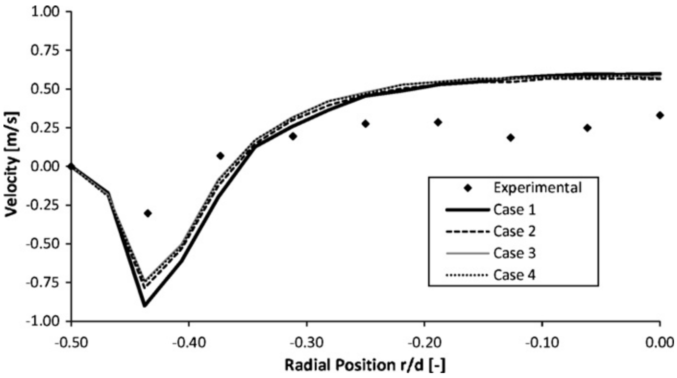

Fig. A.1. Particle velocity across the riser at 0.16 m for the four different meshes in Table A.1 for $\varphi = 0$, $d_p = 60\,\mu\mathrm{m}$ and $V = 0.36\,\mathrm{m\,s^{-1}}$.

Table B.2
Comparison of the computational times of the two drag models for 2D and 3D simulations.

	Time taken (h)	
Drag model	Two-dimensional	Three-dimensional
Gidaspow	≈ 144	≈ 528
EMMS	≈ 192	≈ 720

Appendix B. Computational efficiency

Table B.1 provides the computational times for the 2D and 3D simulations run over 6 processors for the simulations using the two drag models to reach complete circulation, i.e. 10.0 s. The EMMS model takes slightly longer to run compared to the Gidaspow model for both the 2D and 3D simulations. However, should a courser grid be used this would reduce significantly. Although the grid for the 3D case was coarser than the 2D case the 3D models still took a much longer period to reach complete circulation due to the increase in computational cells. To reduce the computational time for 2D and 3D simulations increasing the number of processors used for calculations is a sensible and viable solution for future studies.

References

[1] A. Samuelsberg, B.H. Hjertager, An experimental and numerical study of flow patterns in a circulating fluidized bed reactor, Int. J. Multiphase Flow 22 (1995) 575–591.
[2] F. Berruti, J. Chaouki, L. Godfroy, T.S. Pugsley, G. Patience, Hydrodynamics of circulating fluidized bed risers: a review, Can. J. Chem. Eng. 73 (5) (1995) 579–602.
[3] W. Ge, J. Li, Macroscale phenomena reproduced in microscopic systems-pseudo-particle modelling of fluidization, Chem. Eng. Sci. 58 (2003) 1565–1585.
[4] S. Benyahia, H. Arastoopour, T.M. Knowlton, H. Massah, Simulation of particles and gas flow behaviour in the riser section of a circulating fluidized bed using

the kinetic theory approach for the particulate phase, Powder Technol. 112 (2000) 24–33.
[5] A. Almuttahar, F. Taghipour, Computational fluid dynamics of high density circulating fluidized bed riser: study of modeling parameters, Powder Technol. 185 (2008) 11–23.
[6] M.J.V. Goldschmidt, J.A.M. Kuipers, W.P.M. van Swaaij, Hydrodynamic modelling of dense gas-fluidized beds using the kinetic theory of granular flow: effect of restitution coefficient on bed dynamics, Chem. Eng. Sci. 56 (2001) 571.
[7] S. Sundaresan, Perspective: modeling the hydrodynamics of multiphase flow reactors: current status and challenges, AIChE J. 46 (2000) 1102–1105.
[8] M.A. van der Hoef, M. van Sint Annaland, N.G. Deen, J.A.M. Kuipers, Numerical simulation of dense gas–solid fluidized beds: a multiscale modeling strategy, Annu. Rev. Fluid Mech. 40 (2008) 47–70.
[9] D. Gera, M. Gautam, Y. Tsuji, T. Kawaguchi, T. Tanaka, Computer simulation of bubbles in large-particle fluidized beds, Powder Technol. 98 (1998) 38–47.
[10] D. Gera, M. Syamlal, T.J. O'Brien, Hydrodynamics of particle segregation in fluidized beds, Int. J. Multiphase Flow 30 (2004) 419–428.
[11] C.H. Ibsen, E. Helland, B.H. Hjertager, T. Solberg, L. Tadrist, R. Occelli, Comparison of multifluid ans discrete particle modelling in numerical predictions of gas particle flow in circulating fluidised beds, Powder Technol. 149 (2004) 29–41.
[12] W. Ge, J. Li, Pseudo-particle approach to hydrodynamics of gas/solid two-phase flow, in: Proceedings of the 5th International Conference on Circulating Fluidized Beds, Science Press, Beijing, 1997, pp. 260–265.
[13] W. Ge, J. Li, Macro-scale pseudo-particle modeling for particle–fluid systems, Chin. Sci. Bull. 46 (18) (2001) 1503–1507.
[14] K. Agrawal, P.N. Loezos, M. Syamlal, S. Sundaresan, The role of meso-scale structures in rapid gas–solid flows, J. Fluid Mech. 445 (2001) 151–185.
[15] D. Gidaspow, R. Bezburuah, J. Ding, Hydrodynamics of circulating fluidized beds: kinetic theory approach, in: Proceedings of the 7th Fluidization Conference, 1992.
[16] M. Syamlal, T.J. O'Brien, Derivation of a drag coefficient from velocity-voidage correlation, in: U.S. Dept. of Energy, Office of Fossil Energy, National Energy Technology Laboratory, Morgantown, West Virginia, April 1987.
[17] Y.C. Wen, Y.H. Yu, Mechanics of fluidization, Chem. Eng. Prog. Symp. Ser. 62 (1966) 100.
[18] B.G.M. van Wachem, J.C. Schouten, C.M. van den Bleek, R. Krishna, J.L. Sinclair, Comparative analysis of cfd models of dense gas–solid systems, AIChE J. 47 (5) (2001) 1035–1051.
[19] T.J. O'Brien, M. Syamlal, Particle cluster effects in the numerical simulation of a circulating fluidized bed, in: A.A. Avidan (Ed.), Preprint Volume for CFB-IV, AIChE, New York, 1993, pp. 430–435.
[20] D.J. Gunn, A.A. Malik, The structure of fluidized beds in particulate fluidization, in: A.A. Dringkenbrug (Ed.), Proceedings of the International Symposiumon Fluidization, Netherlands University Press, Eindhoven, The Netherlands, 1967, pp. 52–65.
[21] S. Benyahia, M. Syamlal, T.J. O'Brien, Extension of hill-koch-ladd drag correlation over all ranges of reynolds number and solids volume fraction, Powder Technol. 162 (2006) 166–174.
[22] R.J. Hill, D.L. Koch, A.J.C. Ladd, The first effects of fluid inertia on flows in ordered and random arrays of spheres, J. Fluid Mech. 448 (2001) 213–241.
[23] R.J. Hill, D.L. Koch, A.J.C. Ladd, Moderate-reynolds-number flows in ordered and random arrays of spheres, J. Fluid Mech. 448 (2001) 243–278.
[24] D.Z. Zhang, W.B. VanderHeyden, The effects of mesoscale structures on the macroscopic momentum equations for two-phase flows, Int. J. Multiphase Flow 28 (2002) 805–822.
[25] D.Z. Zhang, A. Prosperetti, Averaged equations for inviscid disperse two-phase flow, J. Fluid Mech. 267 (1994) 185–219.
[26] D.Z. Zhang, A. Prosperetti, Momentum and energy equations for disperse two-phase flow and their closure for dilute suspensions, Int. J. Multiphase Flow 23 (1997) 425–453.
[27] J. De, Wilde, Reformulating and quantifying the generalized added mass in filtered gas–solid flow models, Phys. Fluids 17 (11) (2005) 113304.
[28] J. De Wilde, G.J. Heynderickx, G.B. Marin, Filtered gas–solid momentum transfer models and their application to 3D steady-state riser simulations, Chem. Eng. Sci. 62 (2007) 5451–5457.
[29] N. Yang, W. Wang, W. Ge, L. Wang, Simulation of heterogeneous structure in a circulating fluidized-bed riser by combining the two-fluid model with the emms approach, Ind. Eng. Chem. Res. 43 (2004) 5548–5561.
[30] J.H. Li, A. Chen, Z. Yan, G. Xu, X. Zhang, Particle–fluid contacting in circulating fluidized beds, in: A.A. Avidan (Ed.), Preprint Volume for CFB-IV, AIChE, New York, 1993, pp. 49–54.
[31] J.H. Li, C. Cheng, Z. Zhang, J. Yuan, A. Nemet, F.N. Fett, The emms model-its application, development and updated concepts, Chem. Eng. Sci. 54 (1999) 5409–5425.
[32] J.H. Li, L. Wen, W. Ge, H. Cui, J. Ren, Dissipative structure in concurrent-up gas–solid flow, Chem. Eng. Sci. 53 (1998) 3367–3379.
[33] V. Jiradilok, D. Gidaspow, R.W. Breault, Computation of gas and solid dispersion coefficients in turbulent risers and bubbling beds, Chem. Eng. Sci. 62 (2007) 3397–3409.
[34] D. Gidaspow, Multiphase Flow and Fluidization, Continuum and Kinetic Theory Descriptions, Academic Press, Inc., 1994.
[35] F. Taghipour, N. Ellis, C. Wong, Experimental and computational study of gas–solid fluidized bed hydrodynamics, Chem. Eng. Sci. 60 (2005) 6857–6867.
[36] J.T. Jenkins, S.B. Savage, A theory for the rapid flow of identical, smooth, nearly elastic, spherical particles, J. Fluid Mech. 130 (1983) 187–202.
[37] P. Johnson, R. Jackson, Frictional-collisional constitutive relations for granular materials, with application to plane shearing, J. Fluid Mech. 176 (1987) 67–93.
[38] V. Mathiesen, T. Solberg, B.H. Hjertager, A numerical study of three-dimensional multiphase flow pattern in a riser, in: J. Werther (Ed.), 6th International Conference on Circulating Fluidized Beds, Würzburg, Germany, August 24–27, 1999.
[39] D.Z. Zhang, W.B. VanderHeyden, High-resolution three-dimensional numerical simulation of a circulating fluidized bed, Powder Technol. 116 (2001) 133–141.
[40] J.A.M. Kuipers, W.P.M. van Swaaij Simulation of three-dimensional (3D) riser flow using kinetic theory of granular flow, in: J. Werther (Ed.), 6th International Conference on Circulating Fluidized Beds, Würzburg, Germany, August 24–27, 1999.
[41] C.H. Ibsen, T. Solberg, B.H. Hjertager, Evaluation of a three-dimensional numerical model of a scaled circulating fluidized bed, Ind. Eng. Chem. Res. 40 (23) (2001) 5081–5086.
[42] J. De Wilde, G.B. Marin, G.J. Heynderickx, The effects of abrupt t-outlets in a riser: 3D simulation using the kinetic theory of granular flow, Chem. Eng. Sci. 58 (2003) 877–885.
[43] R.C. Darton, R.D. LaNauze, J.F. Davidson, D. Harrison, Bubble growth due to coalescence in fluidised beds, Trans. Instn. Chem. Engrs. 55 (1977) 274.
[44] D.G. Schaeffer, Instability in the evolution equations describing incompressible granular flow, J. Diff. Equ. 66 (1987) 19–50.
[45] C.K.K. Lun, S.B. Savage, D.J. Jeffrey, N. Chepurniy, Kinetic theories for granular flow: inelastic particles in couette flow and slightly inelastic particles in a general flow field, J. Fluid Mech. 140 (1984) 223–256.
[46] S. Chapman, T.G. Cowling, The Mathematical Theory of Non-Uniform Gases, 3rd edition, Cambridge University Press, Cambridge, UK, 1970, pp. 249–254.
[47] S.A. Vasquez, V.A. Ivanov, A phase coupled method for solving multiphase problems on unstructured meshes, in: Proceedings of ASME FEDSM'00: ASME 2000 Fluids Engineering Division Summer Meeting, Boston, 2000.
[48] J.R. Grace, J. Tuot, A theory for cluster formation in vertically conveyed suspensions of intermediate density, Trans. Inst. Chem. Eng. 57 (1979) 49–54.